3.1 Introduction

$SrTiO_3$-based material is one of the promising material for widespread applications in electronics, energy storage devices, catalysts, dielectric amplifiers [94]–[98], oxygen sensors, humidity sensors [99], [100] and anodes or interconnects for solid oxide fuel cells (SOFCs) [89], [101], [102]. The perovskite structure of $SrTiO_3$ is stabilized in a cubic unit cell with space group $Pm\bar{3}m$ at room temperature. The ionic radii of the elements under doping play an important role [103] in order to maintain a cubic structure. The substitution of donor impurity increases the electrical conductivity of $SrTiO_3$ that may be utilized for anode materials for SOFCs [104].

The substitution of La in $SrTiO_3$ system is found to be effective in increasing the electrical conductivity [105], [106]. The O-2p orbitals and empty conduction band from Ti-3d orbitals make the electronic energy band of $SrTiO_3$ exhibiting an n-type semiconducting behaviour due to redox coupling of Ti^{4+}/Ti^{3+} ions, which increases the electrical conductivity of the system [107]. The substitution of La^{3+} ions on Sr^{2+} sites creates a situation of charge imbalance due to the difference in valence between La^{3+} and Sr^{2+} ions. The introduction of La on Sr site leads to lattice defect structure, which could be modified to maintain charge-neutrality condition [66]. It is also reported that on n-type doping (i.e. with La^{3+} or Nb^{5+}), $SrTiO_3$ becomes a conductor with a low temperature mobility. In this regime, the charge carriers interact with the lattice and behave as polarons [108].

It is reported that there is a lack of reproducibility of conductivity and structural data [109]. Some authors have reported the increase in lattice parameters [110] with La content while some have reported the decrease of lattice parameters with La content

[111]. Hence an attempt has been made to synthesize La-doped $SrTiO_3$ specimens using solid state reaction technique.

In present chapter, the large polaron hopping phenomenon in La-doped $SrTiO_3$ with few compositions of $La_xSr_{1-x}TiO_{3-\delta}$ (with x = 0.0, 0.1, 0.2, 0.3, and 0.4) system which were synthesized via solid state reaction route have been discussed. The conductivity spectra of $La_xSr_{1-x}TiO_{3-\delta}$ (LST) (with x = 0.0, 0.1, 0.2, 0.3 and 0.4) system at different temperatures have been analysed using Jonscher's power law and Ghosh scaling model. This paper aims to analyse the temperature and frequency dependent electrical conductivity of $SrTiO_3$ doped with lanthanum. The validity of the Ghosh scaling model has been studied to explain the dynamics of the charge carriers in the system. The experimental verification of overlapping large polaron conduction mechanism deduced from temperature dependent conductivity spectra and Photoluminescence analysis of LST system have also been reported.

3.2 Results and Discussion

3.2.1 Structural Studies

In the discussion of this chapter, the system $La_xSr_{1-x}TiO_{3-\delta}$ is designated as LST and the compositions with x = 0.0, 0.1, 0.2, 0.3 and 0.4 of this system are assigned as LST0, LST1, LST2, LST3 and LST4, respectively. Figure 3.1 shows the XRD patterns of all sintered LST samples. All diffraction peaks can be indexed to the cubic $SrTiO_3$ perovskite structure with lattice parameter, a = 0.3905 nm, our finding corroborates with the reported data (JCPDS Card Number: 86-0178 ($SrTiO_3$)) [40], [112], [113]. The abbreviations of different compositions of LST system, lattice parameters, cell volume, and crystallite size with lattice strain estimated from the XRD patterns are listed in table 3.1. From this table, it is observed that the unit cell volume decreases with increase in La

content, which may be attributed to the replacement of the larger sized Sr^{2+} ions (1.44 Å, CN 12) at A-sites of the perovskite structure by the smaller La^{3+} ions (1.36 Å, CN 12) [114]. The solubility limit for the composition is 20 mol % as secondary phases start appearing after x = 0.2. Above this composition, peaks of some undesired phases of TiO_2 (JCPDS Card Number: 89-6975 (TiO_2)) start to appear as shown in the fig. 3.1 (d and e). There is no significant change observed in lattice parameters which is in well agreement with Nasrallah et al [115].

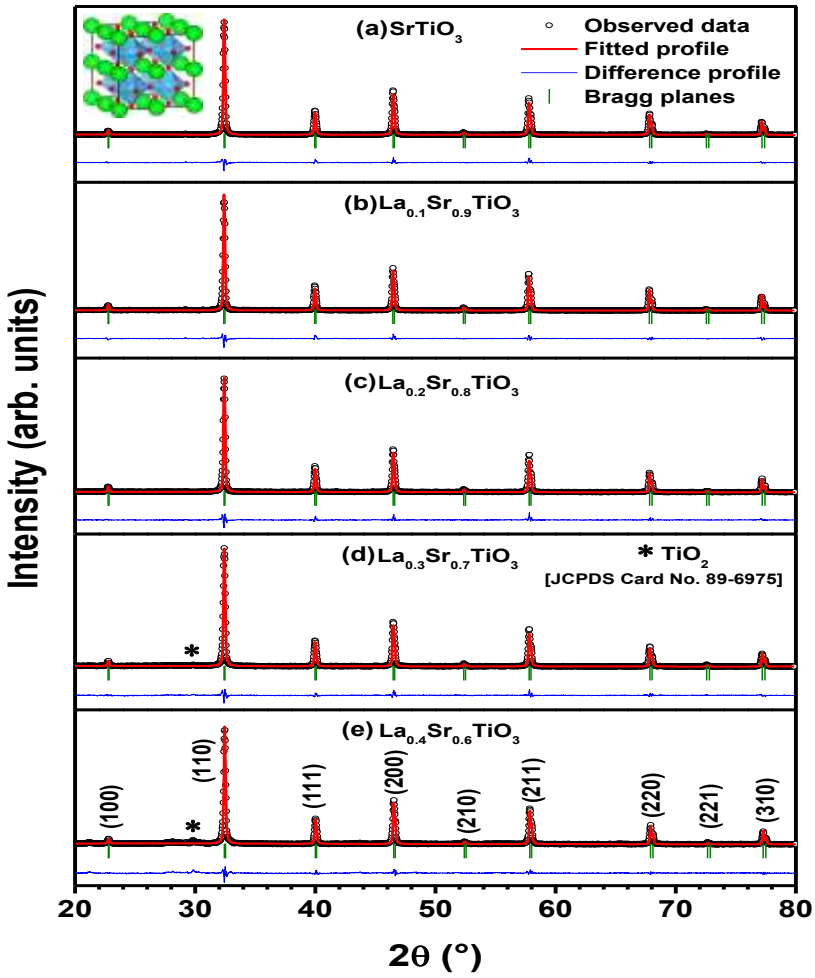

Figure 3.1: Rietveld refinement of X-ray diffraction pattern of $La_xSr_{1-x}TiO_3$ ($0.0 \leq x \leq 0.40$) system sintered at 1400 ºC.

As per Vegard's law, lattice parameters increase from $SrTiO_3$ to $LaTiO_3$ [116] and is dependent on the sintering temperature. With the increase in La content, sintering

temperature for proper densification and lattice formation also increases. Sintering temperature for x = 0.3 composition was found to be optimised at 1650 ºC. Whereas, in the present case, all the samples are sintered at 1400 ºC, hence, the lattice parameters did not show much appreciable change. To investigate the effect of doping on crystal structure, Rietveld analysis of XRD pattern has been carried out using Pseudo-Voigt wave function. The background of each profile was approximated by a 6^{th} order polynomial.

The R_{wp} (weighted-pattern factor) and S (goodness-of-fit) parameters were used as numerical criteria of the quality for the fit of calculated to experimental diffraction patterns. The goodness of fitting parameters is listed in table 3.1.

Table 3.1: Structural parameters, relative density and the goodness of fitting parameters of the LST system.

Sample	**Lattice Parameter (Å)**	**Cell Volume ($Å^3$)**	**Average crystallite size (nm)**	**Average lattice strain ($x10^{-4}$)**	χ^2	$R_{exp.}$	R_B	R_F	**Sr/La -O (Å)**	**Ti-O (Å)**	**Relative density (%)**
LST0	3.9055	59.572	41.57	23.33	6.37	6.85	2.331	1.734	2.7616	1.9528	96
LST1	3.9060	59.594	43.26	22.33	6.58	7.11	2.742	2.135	2.7620	1.9530	88.2
LST2	3.9044	59.521	43.72	22.33	6.83	7.61	3.723	3.072	2.7608	1.9522	88.2
LST3	3.9039	59.501	41.39	23.33	7.95	8.36	6.092	4.278	2.7605	1.9520	84
LST4	3.9007	59.353	41.75	23.33	11.40	9.08	9.162	6.275	2.7582	1.9504	82

At room temperature, $SrTiO_3$ stabilizes in high symmetry cubic $Pm\bar{3}m$ space group. Therefore, refinement of XRD patterns using high symmetry space group could be a good start. Hence, patterns were analysed using $Pm\bar{3}m$ space group and induced

structural distortion can be calculated with La^{3+} ion doping. The goodness of fitting χ^2 becomes poor with the increasing La content.

3.2.2 Density and Micro Structural Studies

The density of the sintered pellets was determined using Archimedes principle and relative density has been found to decrease with the increase in La content (table 3.1) indicating unfavourable condition for densification in the LST samples. As mentioned earlier, higher La content specimens need to be sintered at high temperature 1923 K. Hence, the higher La content specimens have low density. Figure 3.2 depicts the SEM images of the fractured surface of all sintered LST pellets. The grain size of the specimens has been measured using ImageJ software through line intercept method. The grain size has considerably been reduced with the increasing La content. For pure $SrTiO_3$ (LST0), dense grains with water mark and lamellar features are observed. Almost porous morphology has been obtained for the doped compositions.

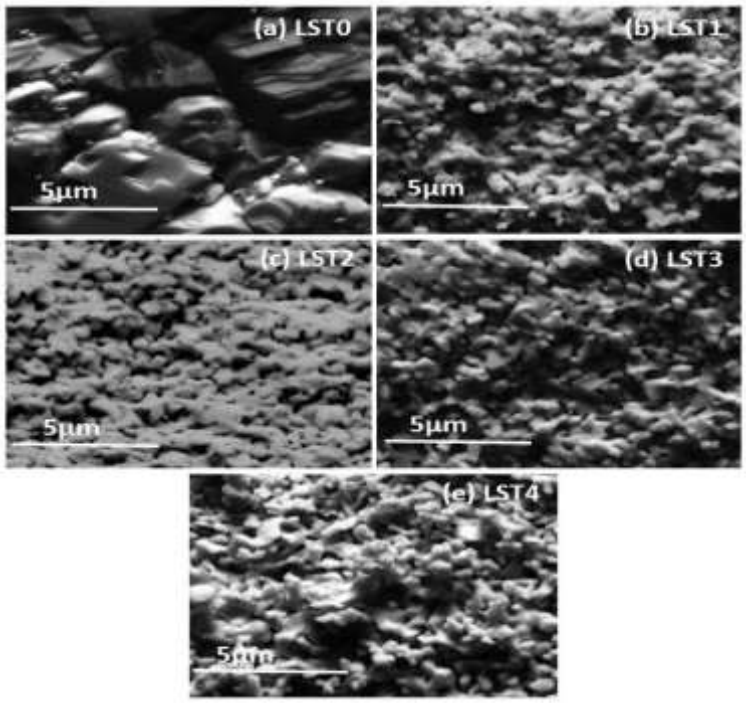

Figure 3.2: SEM image of fractured surface of the sintered pellet of the compositions (a) LST0 (b) LST1 (c) LST2 (d) LST3 and (e) LST4.

3.2.3 Electrical Conductivity

The structural and microstructural studies indicate that the sample LST4 shows secondary phases. Hence, it was excluded from the electrical conductivity measurements. Figure 3.3 depicts the frequency dependent conductivity spectra of the LST samples 400 °C to 600 °C except for $SrTiO_3$, where data is recorded in the temperature range of 460-600 ^oC exhibiting both low and high-frequency dispersion phenomena. The real part of the total conductivity and the Jonscher's power law can be demonstrated by the equations (2.8), (2.9) and (2.10) with the hopping frequency as given by:

$$v_{\mathrm{H}} = \left(\frac{\sigma_{dc}}{A}\right)^{1/n} \tag{3.1}$$

It is the onset of conductivity dispersion in the conductivity spectra. Equation (2.10) is also known as the Almond and West representation of Jonscher's power law [117]–[119]. From this, we can get the hopping frequency and the factor A which is a function of number of sites and hopping length of the consecutive jumps.

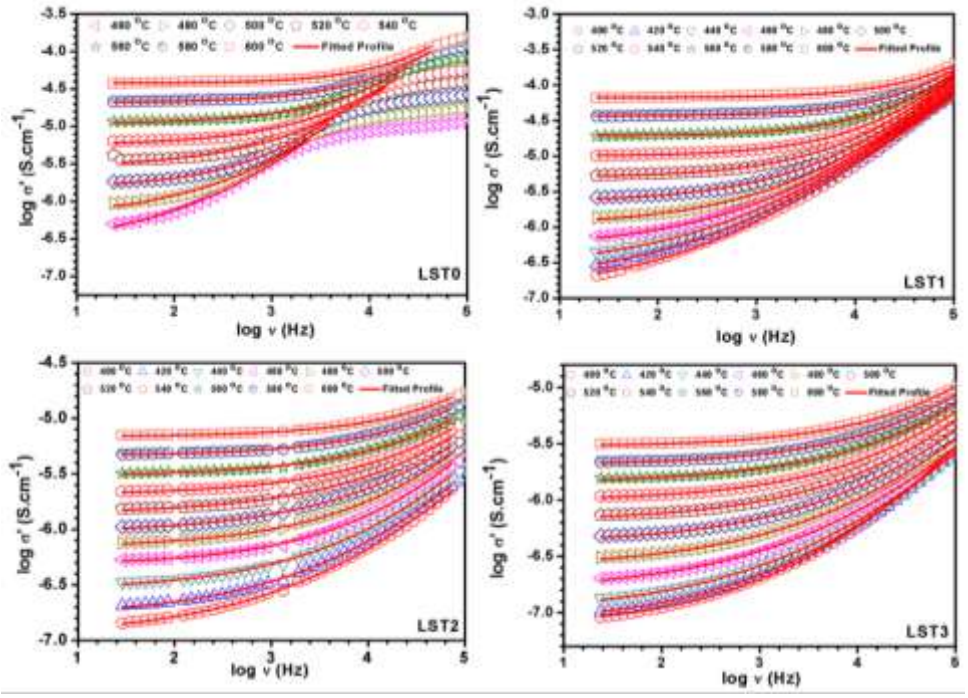

Figure 3.3: Frequency dispersion of Conductivity spectra for LST0, LST1, LST2 and LST3 compositions in the temperature range from 400 ºC to 600 ºC.

The conductivity spectra of all the compositions at different temperatures were fitted with eq. (3.1) as shown in fig. 3.3 for LST0, LST1, LST2 and LST3 compositions. In fig. 3.3, the symbols represent the experimental data points and the solid lines represent the non-linear curve fitting using eq. (3.1). The frequency independent conductivity is a measure of long-range transport of the carrier ions in response to the electric field associated to the successful jump between the two sites.

Figure 3.4 represents the Arrhenius plot of dc conductivity obtained from the fitting of ac conductivity spectra with eq. (2.10) for LST compositions up to $x \leq 0.3$. The dc conductivity of LST system can be described by Arrhenius equation:

$$\sigma_{dc}T = \sigma_o \exp\left(\frac{-E_a}{KT}\right) \tag{3.2}$$

where, σ_o, E_a, k and T are the pre-exponential factor, activation energy, Boltzmann constant and absolute temperature, respectively. The electrical conductivity and activation energy of LST compositions up to $x \leq 0.3$ are listed in table 3.2.

Table 3.2: Electrical conductivity and Activation energy of the LST system.

Sample	**Electrical Conductivity ($S.cm^{-1}$) at 700 °C**	**Activation Energy (eV)**
$SrTiO_3$	3.82×10^{-5}	2.00
$La_{0.1}Sr_{0.9}TiO_3$	6.93×10^{-5}	1.96
$La_{0.2}Sr_{0.8}TiO_3$	6.93×10^{-6}	1.12
$La_{0.3}Sr_{0.7}TiO_3$	3.08×10^{-6}	1.22

Figure 3.4 clearly depicts that the dc conductivity of LST system first increases up to $x = 0.1$ and thereafter (for $x \geq 0.2$) decreases for other compositions. The conductivity of the samples is defined as the sum of electronic and ionic contributions i.e.

$$\sigma = q(n_e\mu_e + n_i\mu_i) \tag{3.3}$$

where n_e, n_i represent the concentration of electrons and ions, μ_e, μ_i represent the electronic and ionic mobility and q represent the elementary charge.

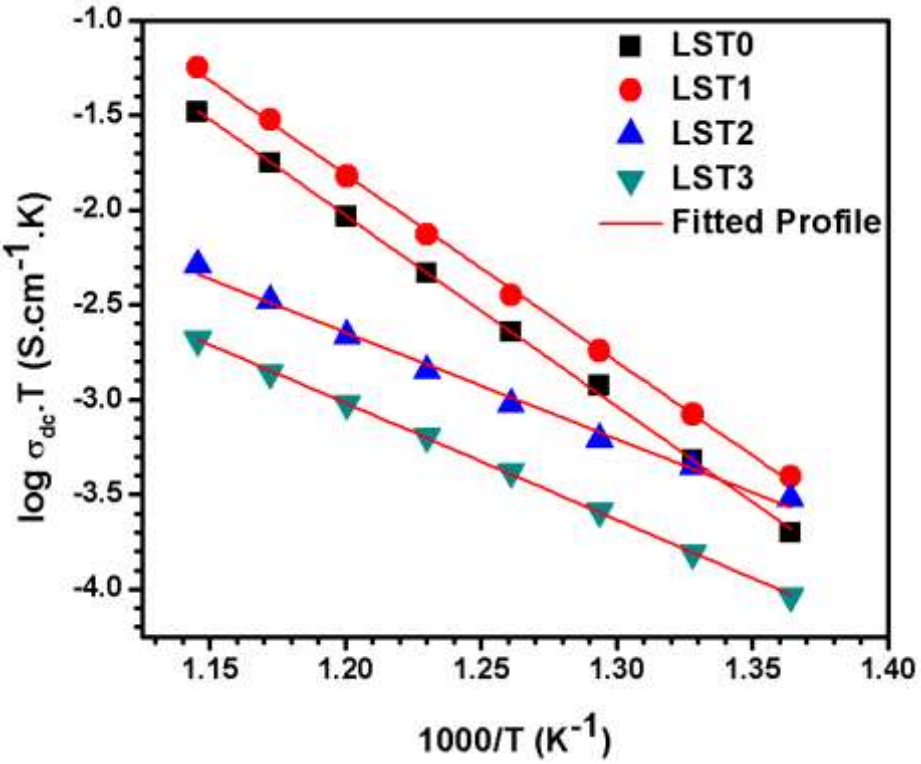

Figure 3.4: Arrhenius Plot of $La_xSr_{1-x}TiO_3$ ($0.0 \leq x \leq 0.30$).

The observed dc conductivity behaviour can be understood by defect chemistry of non-stoichiometric donor doped strontium titanate. The Sr sites commonly occupied by La atoms cause an electronic compensation represented by the following Kröger-Vink equation as:

$$SrO \xrightarrow{La_2O_3} 2La_{Sr}^{\bullet} + 2e' + 2O_O^X + \frac{1}{2} O_2 \uparrow \qquad (3.4)$$

The electrons generated in this process increase the electrical conductivity. For the higher concentrations i.e. for $x > 0.1$, the conductivity is found to decrease. This may be due to the increased scattering of the charge particles [120], [121]. The increasing concentration of the dopant increased the scattering centres, which further leads to the decrease in the mobility of the charge carriers and consequently results in decrease in

conductivity. In stoichiometric La doped $SrTiO_3$, the conductivity depends on the concentration and mobility of free charge carriers, which has been modified with the La content.

3.2.4 Conduction Mechanism

To study the conduction mechanism, exponent *n* obtained from the fitting of conductivity spectra using eq. (2.10), has been plotted with temperature for all the studied samples (fig. 3.5). It is observed that in La substituted samples, the value of n decreases, reaches a minimum, and then further starts increasing. It is well known that if *n* shows an increasing trend as a function of temperature then conduction mechanism is attributed to small polaron tunnelling (SPT) [110], [111]. In contrast with the (non-overlapping) small polaron case, it is found that the value of *n* decreases with temperature reaches a minimum and then increases which indicates overlapping large polaron tunnelling (OLPT). Whereas, temperature independent exponent *n* is attributed to the quantum mechanical tunnelling (QMT) [122]. On the other hand, a decreasing value of *n* with temperature corresponds to correlated barrier hopping phenomena (CBH) [122]. In the present case, the behaviour of *n* with temperature indicates the possibility of formation of overlapping-large polarons in LST system.

It has already been reported that conduction in pure $SrTiO_3$ is due to small polaron tunnelling mechanism [123]. Whereas, in the present case, it can be seen that for a particular temperature range, the value of exponent increases with temperature showing small polaron tunnelling mechanism. With the substitution of lanthanum, it is observed that the value of exponent decreases and approaches a minimum value. Further, it increases with the increase in temperature. This is a signature of formation of large polarons and can be explained on the basis of overlapping large polaron tunnelling model. This indicates a transition in the conduction mechanism from small polaron to large

polaron hopping with the substitution of La. The polaron formation is enhanced by the formation of defect levels which is susceptible to temperature and the dopant concentration [124]. The defects sites almost remain non-interacting over few inter-atomic distances (hopping length). Therefore, with large value of hopping length the conductivity is expected to decrease with increasing temperature. With the increasing hopping length of polaron, large activation energy is needed to hop to nearest neighbour sites [110], [111], [122]. Hence, the large activation energies observed in table 3.2 may be attributed to the polaron conduction.

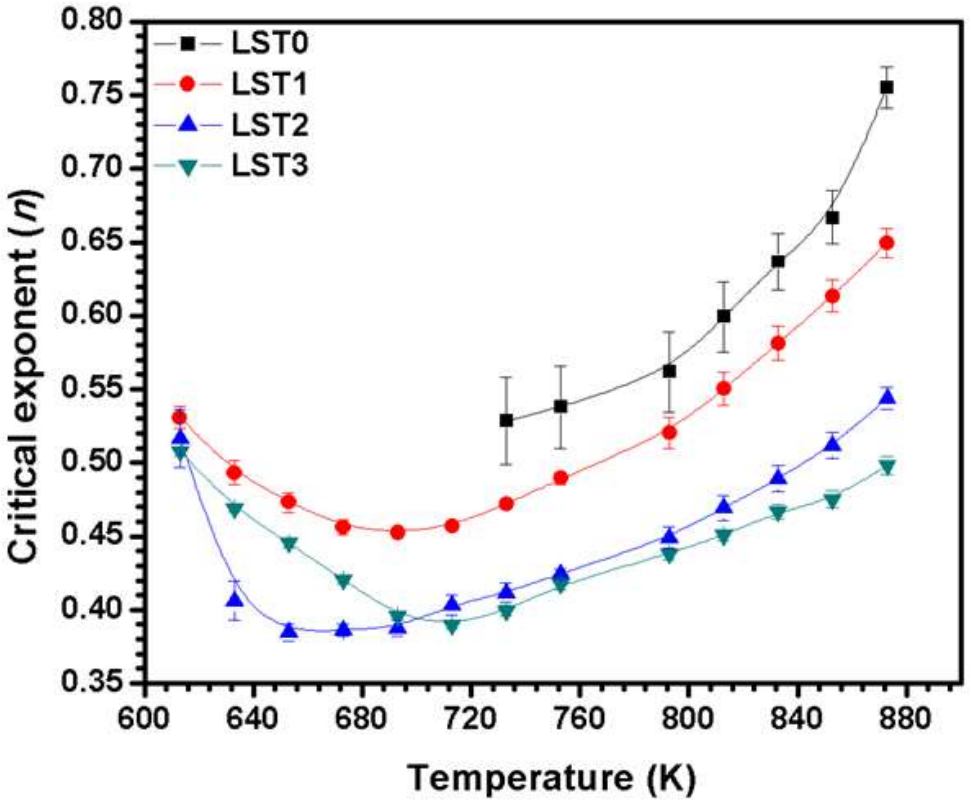

Figure 3.5: Variation of critical exponent n in $La_xSr_{1-x}TiO_3$ ($0.0 \leq x \leq 0.30$) compositions as a function of temperature.

To understand the ion dynamics of the studied samples, scaling behaviour has been studied using Ghosh scaling law with hopping frequency as the scaling factor. Figure 3.6 shows the scaling behaviour of samples under investigation fitted very nicely by Ghosh

scaling with hopping frequency (ν_H) as scaling parameter. The scaling model is described by equation [125], [126]:

$$\sigma(\nu)/\sigma_{dc} = F\,(\nu/\nu_H) \qquad (3.5)$$

The conductivity spectra were found to follow the time temperature superposition (TTSP) principle with slight deviation observed due to window effect [127] in a limited frequency range.

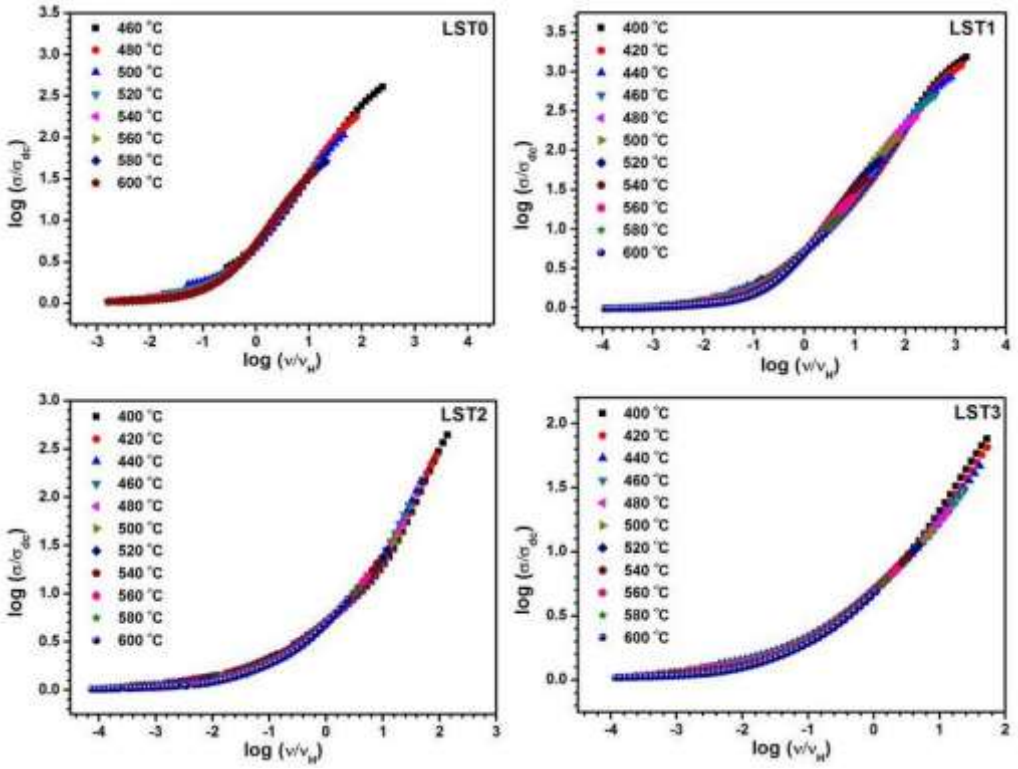

Figure 3.6: Scaled conductivity spectra of the compositions (a) LST0 (b) LST1 (c) LST2 and (d) LST3 in the temperature range from 400 ºC to 600 ºC.

Further, to establish the correlation between bulk conductivity (σ_{dc}) and hopping frequency (ν_H) in all samples, logarithmic plot between these two parameters, obtained from power law fitting, is shown in fig. 3.7. The data follow the linear relationship in all samples within the measured temperature range with slope close to unity. This suggests the degree of correlation between dc and ac conduction mechanisms present in the samples. Such type of correlation was also observed in $LaAlO_3$ based electrolyte [127].

Also, the superposition of different spectra to a master curve for LST system may be a result of constant dimensionality of the conduction network [128].

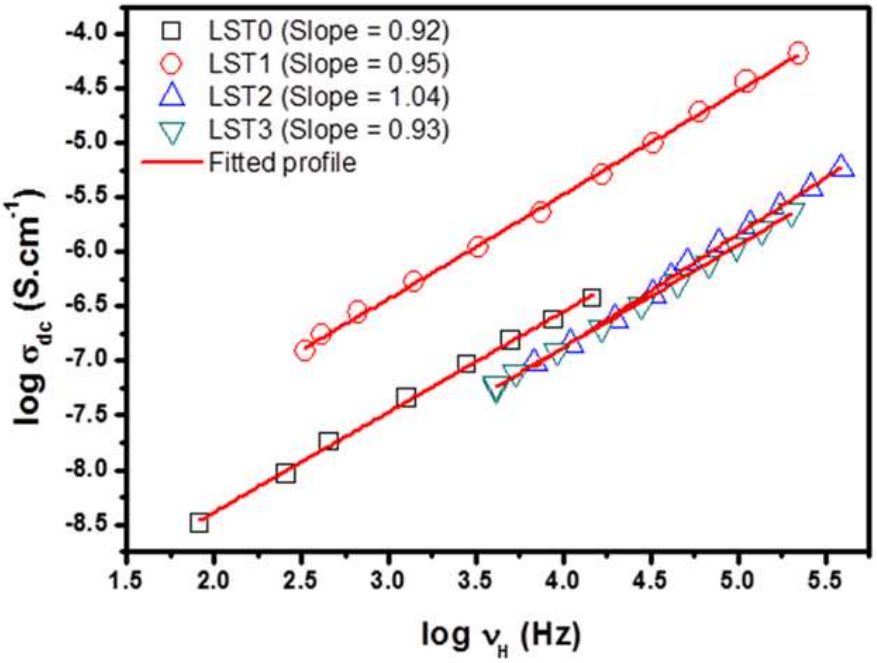

Figure 3.7: The dc conductivity (σ_{dc}) vs. hopping frequency (υ_H) for LST0, LST1, LST2 and LST3 compositions.

3.2.5 Modulus Analysis

The plots of M* and Z* versus frequency distinguishes the long range and short range movement of charge carriers in a relaxation process [129], [130]. Hence, for clarification of the formation of large polarons, M″ and Z″ have been plotted with log (υ). Figure 3.8 shows the variation of M″ and Z″ with log (υ) for (a) LST0, (b) LST1 and (c) LST2 compositions. It is well known that the separation of asymmetric peaks of M″ and Z″ with frequency is attributed to short range hopping of charge carriers and departs from an ideal Debye type behaviour while the coincidence of the frequencies corresponds to long range hopping of charge carriers [131]. It is observed in fig. 3.8 (a) that there is mismatch of asymmetric relaxation peaks *i.e.* peaks of M″ and Z″ do not coincide with each other in LST0 composition. Figure 3.8 (b) indicates that the peak of Z″ and hump of M″ nearly coincide with each other for LST1. Figure 3.8 (c) depicts the formation of

asymmetric peaks in the studied temperature range for LST2 composition. As the peaks are broad and asymmetric, hence should not contain a single peak. To analyse the position and number of peaks the data has been fitted with multi-peak fit using Origin software. It is observed that the peak of Z'' and M'' have achieved the best fit using two peak positions and those peaks are nearly coinciding with each other. Hence, these figures show the formation of small polarons in LST0 and large polarons in La substituted samples with $0.1 \leq x \leq 0.3$.

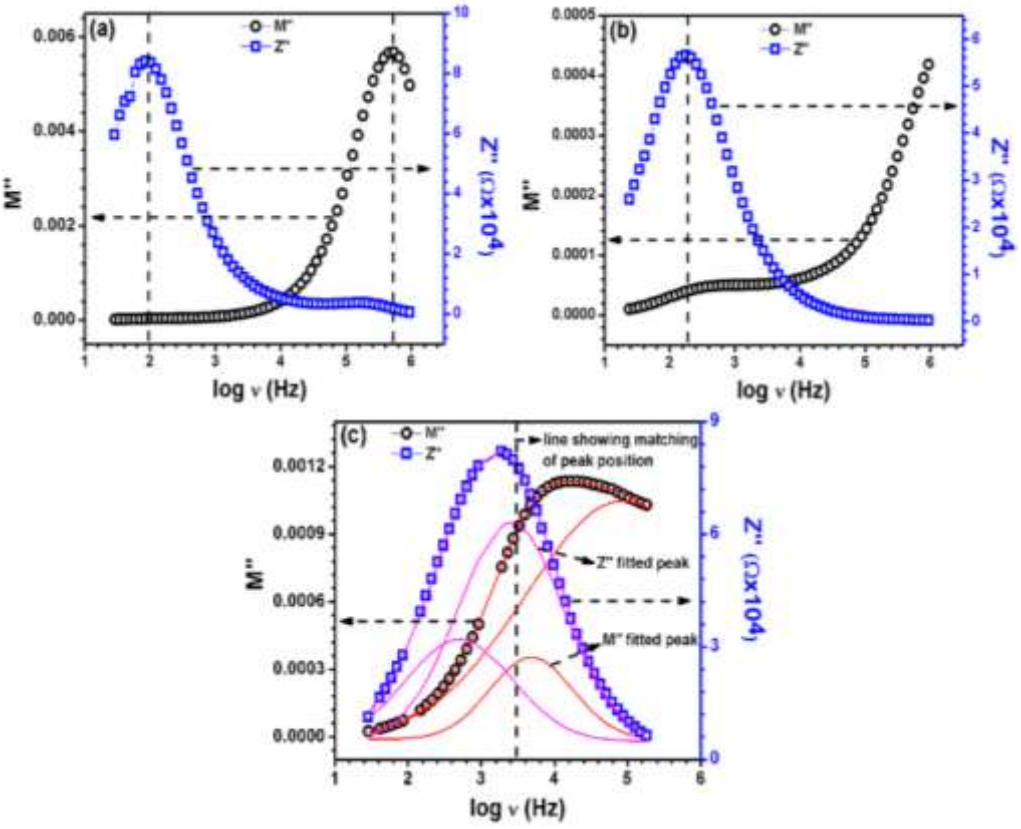

Figure 3.8: Variation of M'' and Z'' with frequency (log ν) for (a) LST0, (b) LST1 and (c) LST2 compositions at 480 ºC.

For the analysis of hopping mechanism, electrical conductivity has been scaled using Power law as discussed earlier. The variation of exponent with temperature reveal the existence of small polaron tunnelling mechanism in LST0 and overlapping large

polaron tunnelling mechanism in La substituted samples. This confirms the conversion from small polarons to large polarons with La substitution.

3.2.6 Photoluminescence Analysis

Photoluminescence (PL) spectroscopy is helpful in studying the order–disorder effects in semiconductors. It also provides opportunity for understanding structural changes in the intermediate-range order. It is well known that impurities, surface states, and defects play an important role in PL properties [132]–[134]. The strong electron–phonon interactions, the formation of polarons and self-trapped excitons, impurities, and defects affect the carrier relaxation processes and carrier recombination dynamics [135], [136]. Hence, for the evidence of polarons, PL emission has been studied. Figure 3.9 depicts the photoluminescence behaviour for La substituted $SrTiO_3$ samples. It is observed that there are four broad emissions: two emissions belong to green region at nearly 2.2-2.4 eV and the other two belong to blue region in the range nearly 2.8-2.9 eV. As known, PL emission is a quantum phenomenon and in order to observe it, there should be certain localized states in the forbidden band gap. Localized states can exist in $SrTiO_3$ crystals if a certain quantity of oxygen vacancies, impurities or tilts are present in the structure. The green emission can be attributed to the decay of self-trapped excitons (STEs). The STE can be depicted as a tightly bound state of a hole and a polaron that can be formed with the oxygen vacancies [137]. Hence this can possibly be correlated to oxygen vacancy assisted polaron conduction. The blue emission is useful for optoelectronic applications and can be attributed to the high-density carriers in the band, which are essential for blue PL [138]. Hence, the mechanism for large polaron conduction has also been confirmed through photoluminescence studies.

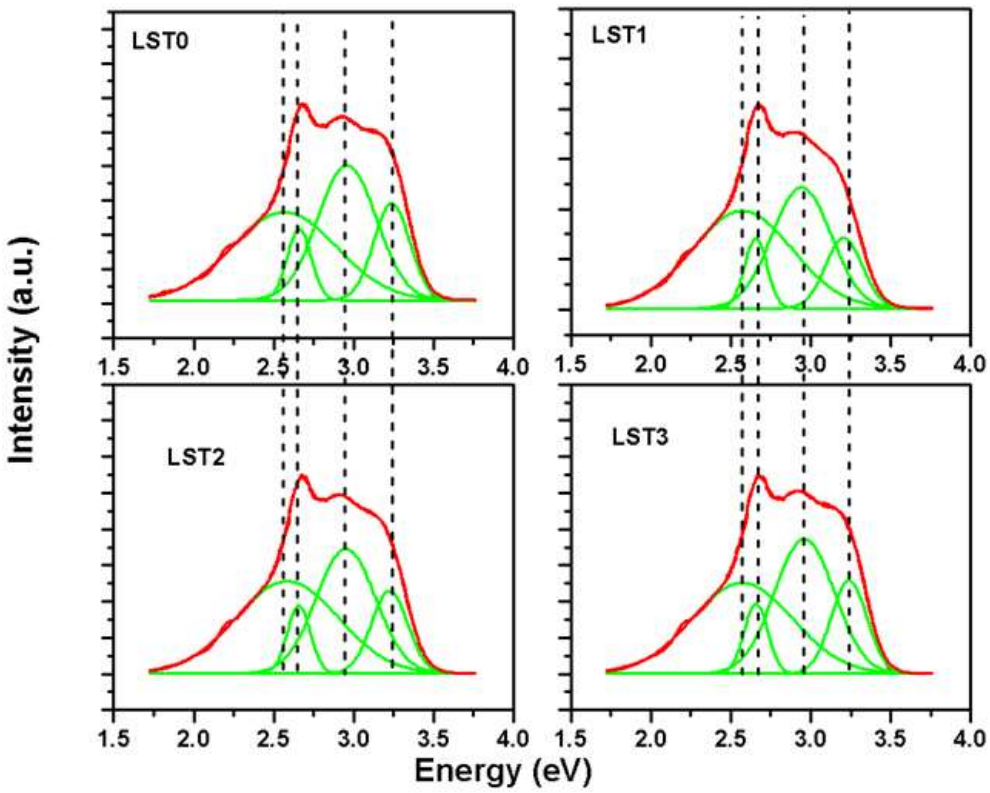

Figure 3.9: Photoluminescence spectra of $La_xSr_{1-x}TiO_3$ ($0.0 \leq x \leq 0.30$) samples.

3.2.7 Evidence of Polaron Size from Structural Data

It is well known that the size of the polarization cloud, called the coherence length, L_{coh}, is smaller than the unit cell dimension a ($L_{coh} < a$), the polaron formed is a small polaron and the polaron formed is a large polaron if $L_{coh} > a$ [139]. To analyse the formation of polarons, firstly the XRD peaks (110) for all the investigated compositions are plotted as shown in fig. 3.10 (a). It is observed that the diffuseness of XRD peak increases with the La substitution. The increase in diffuseness is attributed to the polarons associated with the Jahn Teller distortion [140]. The coherence length of polarons, microstrain and crystallite size have been calculated from XRD results by using Williamson-Hall model [82] as given by eq. (2.1).

Figure 3.10 (b) shows the variation of microstrain and crystallite size with the composition. It is observed that value of microstrain and crystallite size showed the

similar trend i.e. they are increasing with the increase in La content. The samples with the smaller grain sizes as shown in fig. 3.2 are characterized by high amounts of microstrain because strain indicates an amount of disorder. To find out the coherence length, for spherical symmetry of grains (assumed), the coherence length depends on the crystallite size as one-third power of the crystallite size [141], $L_{coh} \approx t^{1/3}$. Figure 3.10 (c) shows the variation of coherence length and lattice constant with the composition. It is observed that for $x \geq 0.1$, the samples L_{coh} is greater than lattice constant, *a*, showing the formation of large polarons. For LST0 (i.e. x = 0.0), the coherence length is smaller than the lattice constant confirming the formation of small polarons.

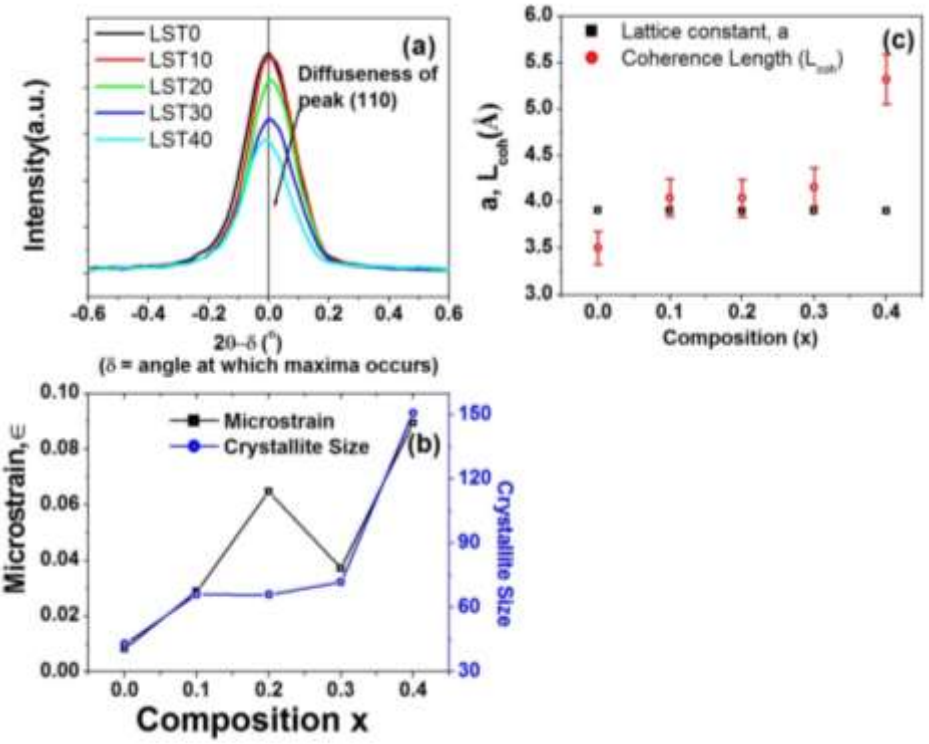

Figure 3.10: (a) Variation of intensity of XRD peak with 2θ-δ (°) where d is the angle at which maxima occurs showing diffuseness of XRD peak (110) with composition, (b) Variation of microstrain and crystallite size with x (c) Variation of coherence length and lattice constant with x.

Further, it is interesting to note that with the increasing La content, the density decreases whereas at the same time the grain size also decreases. This shows contradictory result. This, in present case, is because of two factors, first the substitution

of large ion (Sr^{2+}, 1.44 Å) by the smaller ion (La^{3+}, 1.36 Å) creating void in the system and hence lowering the density. The second reason can be understood from the microstrain data shown in fig. 3.10 (b) indicating that microstrain increases with the La content. The decrease in grain size could be attributed to the increase in microstrain.

3.3 Conclusions

In this chapter, the structural, micro-structural and electrical properties of La-doped $SrTiO_3$ based systems, $La_xSr_{1-x}TiO_{3-\delta}$ (with x = 0.0, 0.1, 0.2, 0.3 and 0.4) have been discussed. The Rietveld refinement of LST system represents cubic phase with space group $Pm\bar{3}m$. The remarkable change in conduction mechanism can be explained on the basis of small polaron and overlapping-large polaron conduction mechanism in La substituted samples. The temperature dependent conductivity spectra for LST samples are found to be superimposed on a single master curve following the Ghosh scaling model with hopping frequency (v_H) as a scaling parameter. The broad blue and green emissions are observed in Photoluminescence spectra, which can be attributed to high-density carriers and self-trapped excitons respectively. Therefore, variation of exponent with temperature, modulus analysis and photoluminescence spectra conclude that the conductivity is because of overlapping large polaron tunnelling conduction mechanism. The size of the polaron is further compared with the lattice parameter and correlated with the coherence length.